Right time, right place: Heterochronicity shapes brain network formation

Francesco Poli[1,2], Stuart Oldham[3,4], Alexia Mousley[1,2], Edward T. Bullmore[2,5], Petra E. Vértes[2], Duncan E. Astle[1,2]

[1]MRC Cognition and Brain Sciences Unit, University of Cambridge, Cambridge, UK

[2]Department of Psychiatry, University of Cambridge, Cambridge, UK

[3]Developmental Imaging, Murdoch Children's Research Institute, The Royal Children's Hospital Melbourne

[4]The Turner Institute for Brain and Mental Health, School of Psychological Sciences and Monash Biomedical Imaging, Monash University, Clayton, Australia

[5]School of Academic Psychiatry, Institute of Psychiatry, Psychology & Neuroscience, King's College London, London UK

Abstract

Brain network formation unfolds on a non-uniform developmental timetable, with different cortical regions generating connections at different developmental phases. Generative network models (GNMs) aim to uncover the principles underpinning the organisation of connectomes by creating synthetic networks according to simple computational rules. These models capture the connectome's topology, operationalised here as the overall distributions of network metrics (e.g., modularity, small-worldness, rich-club structure). However, they typically ignore the differential timing of connectivity formation. By omitting this temporal programme, GNMs often misplace topological features in physical space. Here, we add a heterochronous growth term to GNMs and use a new model fitness function that weighs topology *and topography* equally. Topography refers to the spatial embedding of the network, the actual anatomical positions of tracts. With these advances, we can generate synthetic networks that more faithfully reproduce the spatial layout of diffusion-MRI connectomes from two independent adult cohorts. Compared with classical, temporally agnostic models, heterochronous simulations improve model fit, accurately locate cortical hubs and modules, and converge on a single caudal-to-rostral gradient of brain maturation. Integrating heterochronicity makes GNMs more faithful to brain development, setting the stage for using them to explain and ultimately predict individual differences in network formation.

Keywords: Connectome; Heterochronicity; Brain Development; Generative Network Modelling.

Introduction

Understanding the structural organisation of the brain is crucial for explaining how distributed neuronal activity supports complex cognitive processes. By mapping the connectome, that is, the ensemble of white-matter tracts connecting distinct brain regions (Bullmore & Sporns, 2009), we can chart the physical scaffolding that underpins information flow across specialized neural circuits. In humans, this organisation is typically studied via non-invasive diffusion-weighted MRI, which reveals hallmark topological features such as a small-world architecture, hierarchical modularity, and rich-club organization (Arnatkeviciute et al., 2021; Bassett & Bullmore, 2006; Oldham & Fornito, 2019; Sporns & Betzel, 2016; Van Den Heuvel & Sporns, 2011). These features are thought to foster efficient communication among distributed brain areas, enabling the emergence of complex cognitive functions. During childhood, the ongoing refinement of large-scale networks accelerates the integration of distinct functional systems, laying the foundation for higher-order cognitive abilities such as language and executive control (Gogtay et al., 2004). By charting how network architecture emerges across time, we gain critical insights into the mechanisms that steer structural maturation. In time, this may advance our understanding of how diversity in brain structure and function emerge, including in those cases where people encounter cognitive or clinical difficulties.

In the last twenty years, generative network models (GNMs) have become a crucial tool for understanding the architecture of brain networks (Kaiser & Hilgetag, 2004a, 2004b; Vértes et al., 2012). GNMs gain their explanatory power by compressing the connectome's complexity into a concise, interpretable set of wiring rules. For instance, many connections can be explained by a "homophily" rule, whereby two brain areas are more likely to connect if they share similar connections to other areas (Sebenius et al., 2025; Vértes et al., 2012). Concurrently, some penalties must be introduced to avoid generating connections that are too costly. For example, generating and maintaining long distance connections would require greater metabolic costs, and this should thus be avoided when possible (Bullmore & Sporns, 2012; Kaiser & Hilgetag, 2004a). In so doing, GNMs can reproduce many topological features of the connectome, such as its modular structure, rich-club architecture, and number of hub regions (Arnatkeviciute et al., 2021; Bassett & Bullmore, 2006; Oldham et al., 2022; Sporns & Betzel, 2016; Van Den Heuvel & Sporns, 2011). GNMs provide a quantitative tool to understand which general rules any plausible wiring process must satisfy, improving also our ability the ability to capture group-differences in disease (Vértes et al., 2012; Zhang et al., 2021) and inter-individual differences (Akarca et al., 2021). However, they are not intended to recreate the full biological mechanisms, or developmental timelines, that give rise to those networks.

While GNMs have successfully reproduced the topology of brain networks, they cannot capture their topographical properties (Oldham et al., 2025). By topography, we refer to the spatial embedding of the connectome, including the exact physical locations of nodes and the spatial arrangement of modules and hubs. This is in contrast to the topology of the network which refers to the pattern of connections between nodes regardless of their spatial location. As a result, even though GNMs can correctly approximate the number of hubs, they often place these hubs in anatomically implausible positions. This illustrates that there is an important conceptual difference between mirroring network topology and replicating the spatial or topographic reality of the brain.

We argue that existing GNMs fail to capture brain topography because their algorithms depart from the biological processes that sculpt neural wiring during development (Akarca et al., 2021; Carozza et al., 2023, 2024). In actual brains, the emergence of new connections during development is not random but follows spatially *heterochronous* patterns of neurodevelopment, which dictate the timing and manner in which neurons are born, migrate, and mature (Goulas, Majka, et al., 2019). Introducing heterochronicity into our models has the potential to capture these spatiotemporal constraints,

thereby overcoming the limitations of existing GNMs. Ultimately, this approach could yield models that more faithfully approximate not only the topology of real brains, but also their topography (Kaiser, 2017; Oldham & Fornito, 2023).

Here, we integrate biologically grounded processes into GNMs to close the gap between developmental mechanisms and computational models of network architecture. Inspired by previous work (Goulas, Betzel, et al., 2019), we mathematically define spatially ordered heterochronous developmental gradients. We hypothesise that this advancement will improve our ability to simulate brain structure. Moreover, this will in turn allow for the testing of hypotheses about the spatio-temporal principles that organise the brain.

One prominent theoretical question to be tested pertains to the 'dual origins' theory of brain organisation (Finlay & Uchiyama, 2015, 2020; Goulas, Margulies, et al., 2019; Pandya et al., 2015; Sebenius et al., 2024; Yeterian et al., 2012), which posits that the mammalian cerebral cortex has evolved along two principal gradients originating from the piriform cortex (paleocortex) and the medial wall, including the hippocampus (archicortex). These two foci of cortical expansion are expected to give rise to anatomically distinct spatial patterns in terms of laminar thickness, neuronal density, and myelination (Pandya et al., 2015). A second theory argues for different origin points, stressing how one neurogenesis gradient should start in the rostrolateral (frontal) region and proceed caudomedially (toward posterior sensory areas). The other origin point should be located in the thalamus, with primary sensory thalamic nuclei (lateral/medial geniculate, ventrobasal nuclei) maturing earliest and projecting to their respective posterior sensory areas sooner (Finlay & Uchiyama, 2020). By introducing additional parameters which vary the number and location of origin points, we can test for any existing model-based evidence in favour of either of these theories.

Results

Computational Advances

We used GNMs to simulate brain network formation (Figure 1A). These synthetic networks were then compared to real brain networks. Usually, the comparison is made using an energy function that considers how well the topological properties of the actual brain network are captured by the synthetic network. By energy, we refer to a single scalar "mismatch" score (lower is better) quantifying how unlike the synthetic and empirical networks are. In the classical formulation, energy is the maximum KS distance between the cumulative distributions of degree, betweenness centrality, clustering coefficient, and edge length.

We expanded this energy score to consider topographical properties as well (Figure 1B). That is, this addition considers not just the overall distribution of those topological properties (as in previous work), but also their spatial alignment with the empirical data. In other words, are hubs and peripheral nodes in the right place, and so on? More specifically, for each node we correlated its degree, betweenness and clustering values in the synthetic versus real network, and took the lowest of those three correlations as the topographical cost (see also *Model Fitting* in the Methods section). Since we aimed to capture the approximate (rather than the accurate) location of these network properties, we carried out a spatial smoothing before correlating the synthetic and real metrics (Figure 1C). We used the new energy score to identify the GNM that produced the best model fit. The classic form of GNMs are composed of two terms, one for value (e.g., homophily) and one for cost (e.g., Euclidean distance) (Betzel et al., 2016; Vértes et al., 2012). Here, we introduce a third term for heterochronicity:

$$\mathrm{P_{i,j,t}} \propto (\mathrm{K_{i,j,t}})^{\eta} (\mathrm{D_{i,j}})^{\gamma} e^{(\lambda \mathrm{H_{i,j,t}})} , \qquad (4)$$

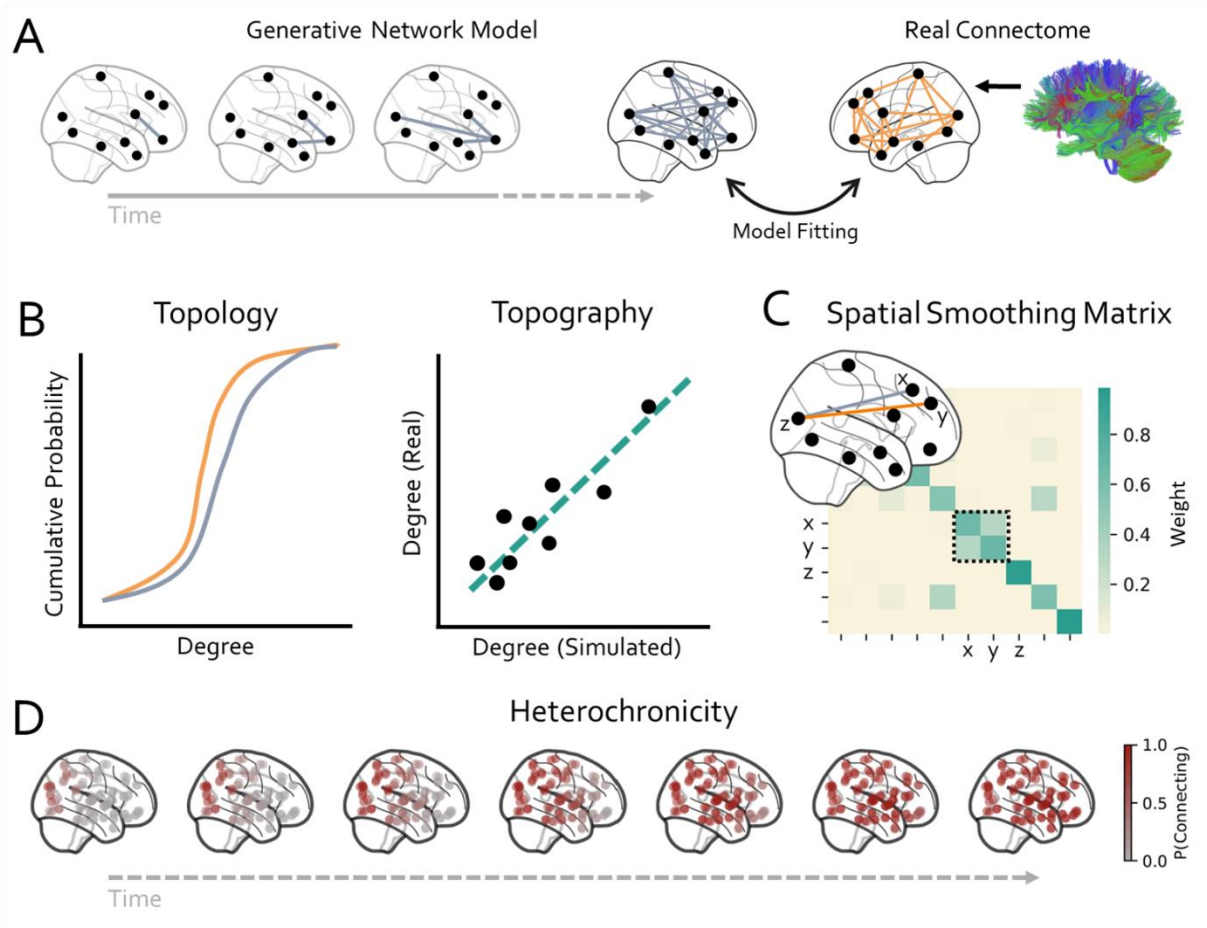

Figure 1. Generative network models simulate brain network formation. A. Starting from an empty graph, edges are generated one by one according to a cost–benefit rule that weighs Euclidean distance against a wiring value such as homophily. The process stops when the synthetic network reaches the density of the empirical connectome, reconstructed from diffusion MRI (streamline count), parcellated with the AAL atlas and binarised. Model parameters are optimised by minimising *energy*—the discrepancy between synthetic and empirical graphs. **B.** Conventional energy functions compare only topology, i.e. the overlap of cumulative distributions of node-level network metrics. We extend this criterion to include *topography*—whether corresponding nodes share similar network metric values—assigning equal weight to both components in the new energy function. **C.** The revised metric also grants partial credit to "near-miss" edges: if the model connects *z* to *x* instead of the empirical *z*–*y* link, the penalty is reduced when *x* and *y* are spatial neighbours. This is implemented by blurring every node's metric with a distance-weighted (Gaussian) smoothing kernel so that neighbouring parcels share some of each other's value. **D.** Example of heterochronous gradient, whereby different areas make connections following a specific spatiotemporal pattern. The probability of a given area (each dot) of establishing connections with any other area is depicted in a grey-to-red scale.

where $\mathrm{P}_{\mathrm{i,j,t}}$ indicates the probability that a connection from node *i* and *j* is made at time *t; K*, *D* and *H* represent the matrices for homophily (i.e., matching index), Euclidean distance, and heterochronicity respectively, and γ, η, and λ represent three parameters regulating the extent to which the three matrices influence wiring probabilities. We refer to this new model as the heterochronous GNM, while the form without the $e^{(\lambda \mathrm{H}_{\mathrm{i,j,t}})}$ term we refer to as the classical GNM.

According to the heterochronicity matrix, H, different nodes start generating connections at different points in time. More specifically, we defined a Gaussian activation wave that started at an origin point (e.g., primary visual cortex in Figure 1D) and gradually swept outward: Nodes closer to the origin

increase their probability of connecting earlier, while those farther away start forming connections later. A formal definition of this heterochronous process is available in the Methods section under Computational Modelling.

Heterochronous models produce better model fit than classical models

We fitted the GNMs with a grid search algorithm with γ, η, and λ as free parameters. Additionally, the origin point of the heterochronicity gradient was left free to vary across the medial axis of the brain, which naturally enforces symmetry. The models were fit to two datasets, the Cambridge Centre for Ageing and Neuroscience dataset (CamCAN) and the Human Connectome Project – young adults dataset (HCPya) (see under *Datasets* in the *Methods* section). More specifically, for all participants between 26 and 35 years of age, white-matter tracts were parcellated using the automated anatomical labeling (AAL) atlas (Rolls et al., 2020). We selected this atlas because its well-validated 90-region resolution consistently recovers canonical connectome features (e.g., small-worldness, rich-club hubs, see Achard et al., 2006; Gong et al., 2009; Mousley et al., 2025) . For GNMs, computing time scales with network size, and AAL is thus computationally more tractable. Next, a consensus network was derived for each dataset (Betzel et al., 2019), thresholding the networks at 10% density (as in Akarca et al., 2021; Betzel et al., 2016). Given the stochastic nature of the generative process, each combination of parameters values generated 10 synthetic networks (i.e., 10 different runs with the same parameters values were performed) (Liu et al., 2023).

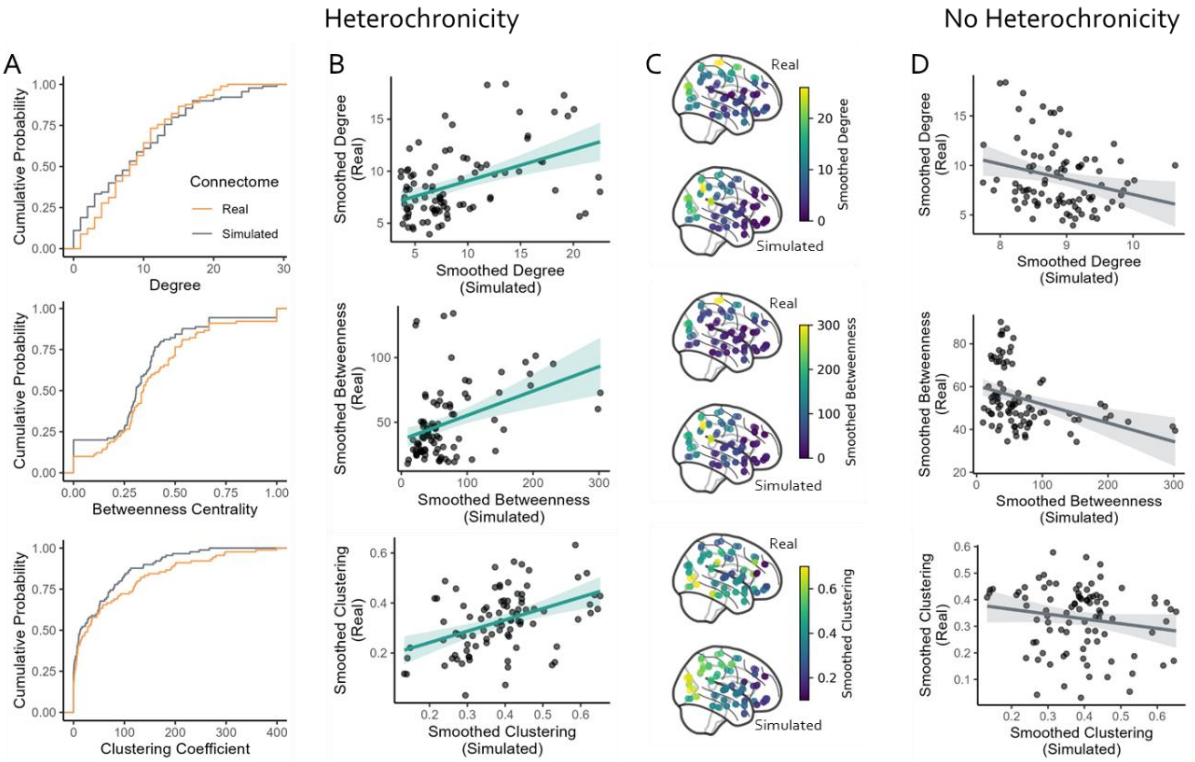

Figure 2. Homophily, heterochronicity, and distance penalty jointly contribute to generating plausible synthetic networks. A. Energy landscapes for each free parameter of the generative model, shown separately for the CamCAN (light) and HCPya (dark) datasets. For every panel, the remaining two parameters are fixed at the combination that yields the global energy minimum. Shaded ribbons denote 95 % confidence intervals across simulation runs. **B.** Global sensitivity analysis: standardised regression coefficients quantify how strongly each parameter contributes to lowering total energy (negative values indicate that larger parameter magnitudes reduce energy). **C.** Heterochronous models lead to significantly lower energy than classical models, indicating better model fit. **D.** Introducing heterochronicity leads to a shift in the trade-off between homphily (weakens) and distance penalty (strengthens).

Results show that all parameters contributed to improve the total energy (Figure 2A-C). More specifically, a sensitivity analysis (Figure 2D; Supplementary Figure 1) showed that γ contributed the most to the decrease in total energy (CamCAN: β = -0.29, SE = 0.01, t = -19.99, p < 0.001; HCPya: β = -0.29, SE = 0.01, t = -20.82, p < 0.001), followed by λ (CamCAN: β = -0.14, SE = 0.01, t = -16.42, p < 0.001; HCPya: β = -0.14, SE = 0.01, t = -16.65, p < 0.001) and η (CamCAN: β = -0.06, SE = 0.01, t = -4.26, p < 0.001; HCPya: β = -0.06, SE = 0.01, t = -4.711, p < 0.001). Crucially, the energy of heterochronous models was significantly lower than the energy of classical models (i.e., when λ = 0) for both datasets (CamCAN: β = -0.08, SE = 0.02, t = -4.55, p < 0.001; HCPya: β = -0.06, SE = 0.01, t = -4.48, p < 0.001) indicating that introducing heterochronicity led to significantly more brain-like network. More specifically, heterochronicity led to a shift in the trade-off between cost (i.e., distance) and value (i.e., homophily), with more negative parameter values for η and weaker positive parameters values for γ. This suggests that the heterochronous gradient actively promotes the formation of connections that are both homophilic and long-range. In turn, this alters the role of the other two model terms: because heterochronicity already drives up homophily, the homophily term η can be reduced without compromising topological fit. Conversely, because the gradient tends to generate more long-distance connections, the distance penalty γ must be increased to restrain the formation of metabolically costly links. In other words, the heterochronous mechanism shifts the balance of the model, requiring less homophily and more cost aversion to reproduce brain-like networks.

Heterochronous models capture brain network topology and topography

Heterochronous models capture brain topology just as well as classical models, with low KS-statistics values for nodal degree (KS = 0.14, p = 0.30), betweenness centrality (KS = 0.14, p = 0.30), and clustering coefficient (KS = 0.17, p = 0.16). However, they perform *better* than classical models in terms

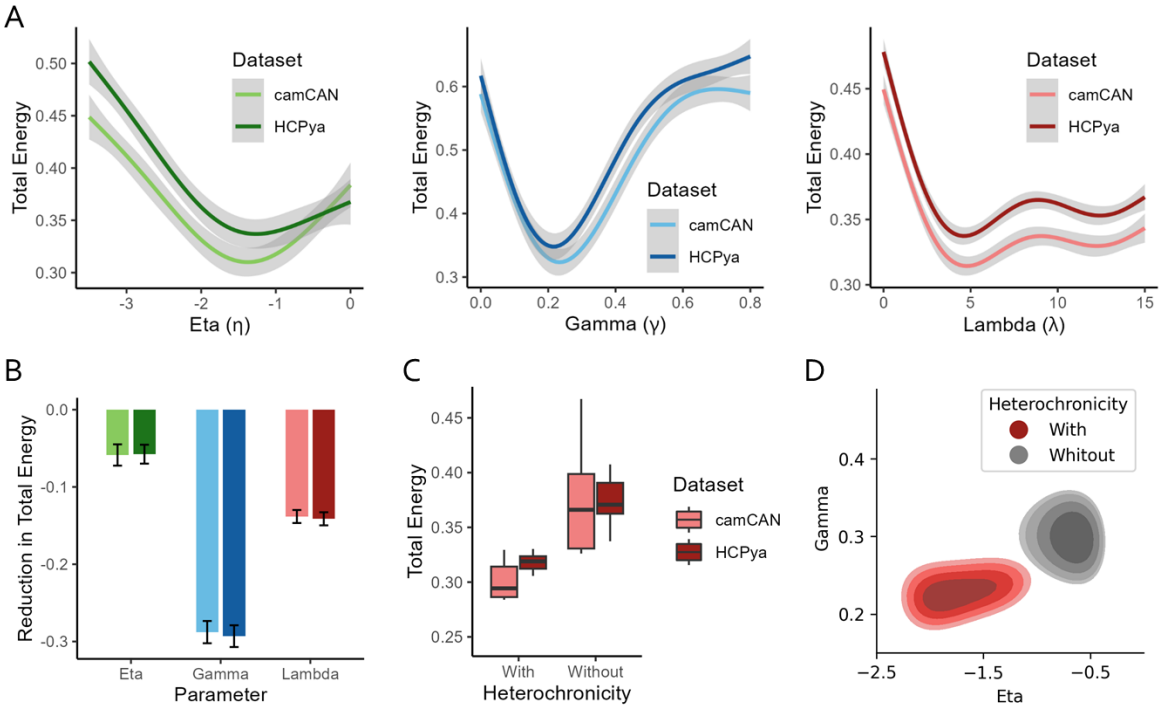

Figure 3. Heterochronous models capture real networks topography. A. Cumulative distributions of nodal degree, betweenness centrality, and clustering coefficient for the empirical connectome (orange) and its best-fitting heterochronous surrogate (grey). The two curves overlap closely for each metric, indicating that the model captures the global statistics (topological properties) of the real network. **B.** For the heterochronous model, vertex-wise values of the three smoothed metrics correlate with their empirical counterparts (solid regression lines, 95 % CI shading). C. Spatial maps of the smoothed metrics in the real brain (upper row of each pair) and the heterochronous surrogate (lower row) further illustrate their alignment. **D.** In contrast, the classical (non-heterochronous) model yields weak or negative correlations with the empirical data and fails to reproduce the observed spatial organization.

of topography. More specifically, we found a positive correlation between the (smoothed) degree of the simulated and real network nodes ($\beta = 0.45$, SE = 0.01, $t = 4.68$, $p < 0.001$), their betweenness centrality ($\beta = 0.40$, SE = 0.01, $t = 4.07$, $p < 0.001$), and their clustering coefficient ($\beta = 0.44$, SE = 0.01, $t = 4.66$, $p < 0.001$). This is in stark contrast with classical models which lack heterochronicity, where no significant correlation between spatial maps of real and simulated nodes was found for clustering coefficient ($\beta = -0.17$, SE = 0.01, $t = -1.63$, $p = 0.107$) and betweenness centrality ($\beta = -0.06$, SE = 0.01, $t = -0.53$, $p = 0.599$), and this correlation was even significantly negative for nodal degree ($\beta = -0.25$, SE = 0.01, $t = -2.46$, $p = 0.016$). Overall, this indicates that introducing a heterochronicity gradient leads to a strong improvement in the model's capacity to mimic brain network topography. Comparable results were found for the HCPya dataset (see supplementary materials).

Inferring the spatial origin of brain network formation

In our main analyses, the origin point of the heterochronicity gradient was free to vary across the medial plane (Figure 4A). Results from the sweep over the medial plane identified the caudal part of the brain as the origin point that reliably produced lower energy scores (Figure 4B; Supplementary Figure 2) for both datasets. That is, when the heterochronous wave starts at this point, the simulations are more brain-like. More specifically, we observe that more caudal origin points led to lower energy (CamCAN: $\beta = 0.04$, SE = 0.002, $t = 24.05$, $p < 0.001$; HCPya: $\beta = 0.04$, SE = 0.002, $t = 24.51$, $p < 0.001$) and more dorsal origin points also led to lower energy (CamCAN: $\beta = -0.03$, SE = 0.002, $t = -16.66$, $p < 0.001$; HCPya: $\beta = -0.04$, SE = 0.002, $t = -22.26$, $p < 0.001$).

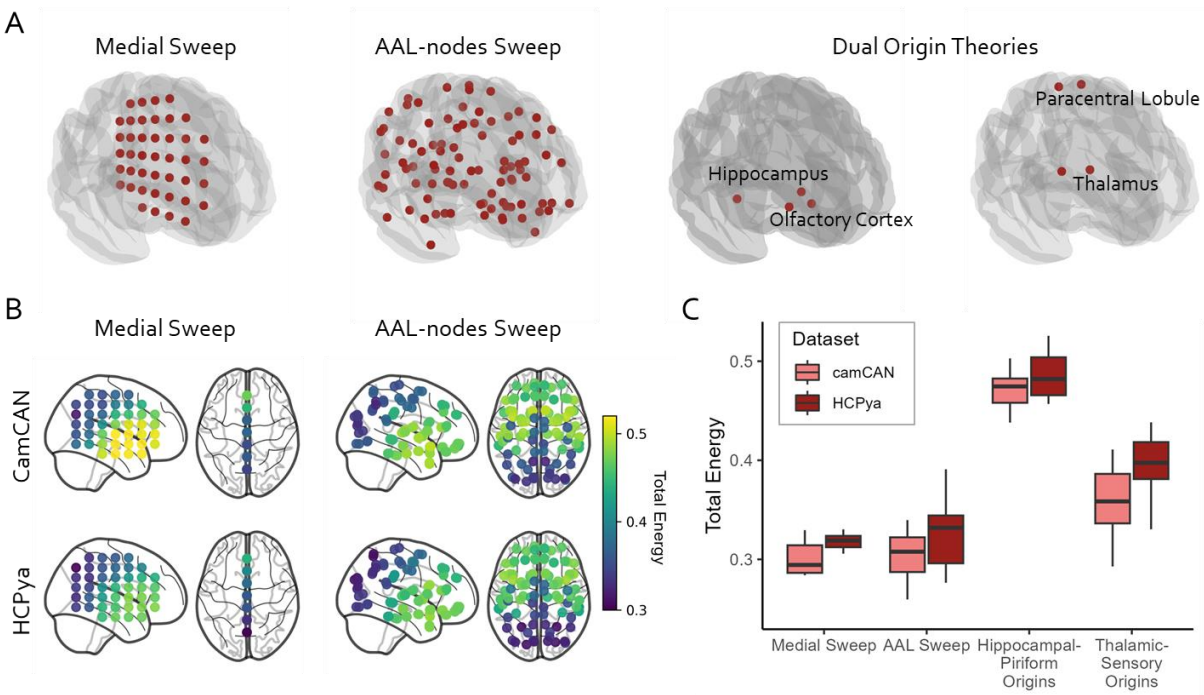

Figure 4. Single-origin heterochronous growth seeded from dorsocaudal cortex best reproduces real networks. **A.** Seed configurations used to initialise heterochronous growth models. Red spheres indicate (i) a systematic "medial sweep", (ii) a sweep across anatomical AAL nodes, and (iii) two dual-origin hypotheses (hippocampal-piriform and thalamic-prefrontal pairs). **B.** Vertex-wise total energy for the medial and AAL sweeps in both datasets. Seeds placed farther dorsally and caudally yield lower energy, implying a closer match to the empirical network's topology and topography. **C.** In both datasets, single-origin models outperform dual-origin models; Lower energy indicates a more accurate synthetic network.

To further probe potential origins of brain network formation, we run additional models manipulating the origin points. First, we performed a sweep over the *x-y-z* coordinates of all AAL nodes. To maintain hemispheric symmetry, the origin point was never starting from a single hemisphere, but always bilaterally. Second, we tested specific theories about the dual origin of the brain. One theory points at hippocampal and olfactory cortices as origin points (Pandya et al., 2015); the other points at the thalamus and sensorimotor cortices as possible origin points (Finlay & Uchiyama, 2020; Figure 4A).

Results from the sweep over the AAL coordinates replicated the initial results, identifying the caudal part of the brain as the origin point that reliably produced lower energy scores for both datasets (Figure 4B). Thus, our model indicates the heterochronicity gradient generally moves from caudal to rostral direction.

When looking at the energy produced by the dual origin models, we saw significantly higher values for both the hippocampal-piriform origin (CamCAN: $\beta = 0.14$, SE = 0.02, $t = 9.06$, $p < 0.001$; HCPya: $\beta = 0.13$, SE = 0.01, $t = 9.68$, $p < 0.001$) and the thalamic-prefrontal origin (CamCAN: $\beta = 0.13$, SE = 0.01, $t = 8.67$, $p < 0.001$; HCPya: $\beta = 0.14$, SE = 0.01, $t = 10.70$, $p < 0.001$), indicating poorer model fit. Hence, at least with the current data type and pre-processing steps (i.e., streamline counts, parcellated in AAL), we do not find evidence in favour of a dual origin of the brain.

Advances and systematic limitations in charting long-range connections

Models incorporating heterochronicity create networks that are more topographically similar to real brains, relative to classical models, but are they doing any better in the number and placement of critical long-range connections? This was a noteworthy failure of classical models (Oldham et al., 2025). To test whether heterochronous models led to any improvements in this regard, we checked differences in the distribution of the lengths of the connections between the real, the standard, and the heterochronous connectomes (Figure 5A-B). By comparing KS-statistics across all runs of the models, we find that the heterochronous connectomes are more similar to the real connectome than the classical ones for CamCAN ($\beta = 0.15$, SE = 0.006, $t = 24.65$, $p < 0.001$), although this difference was not significant for HCPya ($\beta = 0.007$, SE = 0.007, $t = 1.00$, $p = 0.324$). This improvement was specifically due to the right tail of the distribution, which concerns long-range connections (see Figure 5A). Hence, the heterochronous model better simulates the correct proportion of long-distance connections, relative to standard GNMs.

Heterochronous models do not simply generate a more faithful distribution of the real connections, but are also more likely to place the connections in the right place. Given that, compared to classical models, heterochronous models are more likely to place connections where they actually exist, and less likely to place them where they do not exist (Figure 5C). However, they perform above chance only for short-range connections. As the length of the connections increases, the probability that these connections are placed in the right place falls to zero (CamCAN: $\beta = -0.04$, SE = 0.001, $t = -24.52$, $p < 0.001$; HCPya: $\beta = -0.05$, SE = 0.002, $t = -30.64$, $p < 0.001$). This systematic limitation of generative network models will be addressed in the discussion.

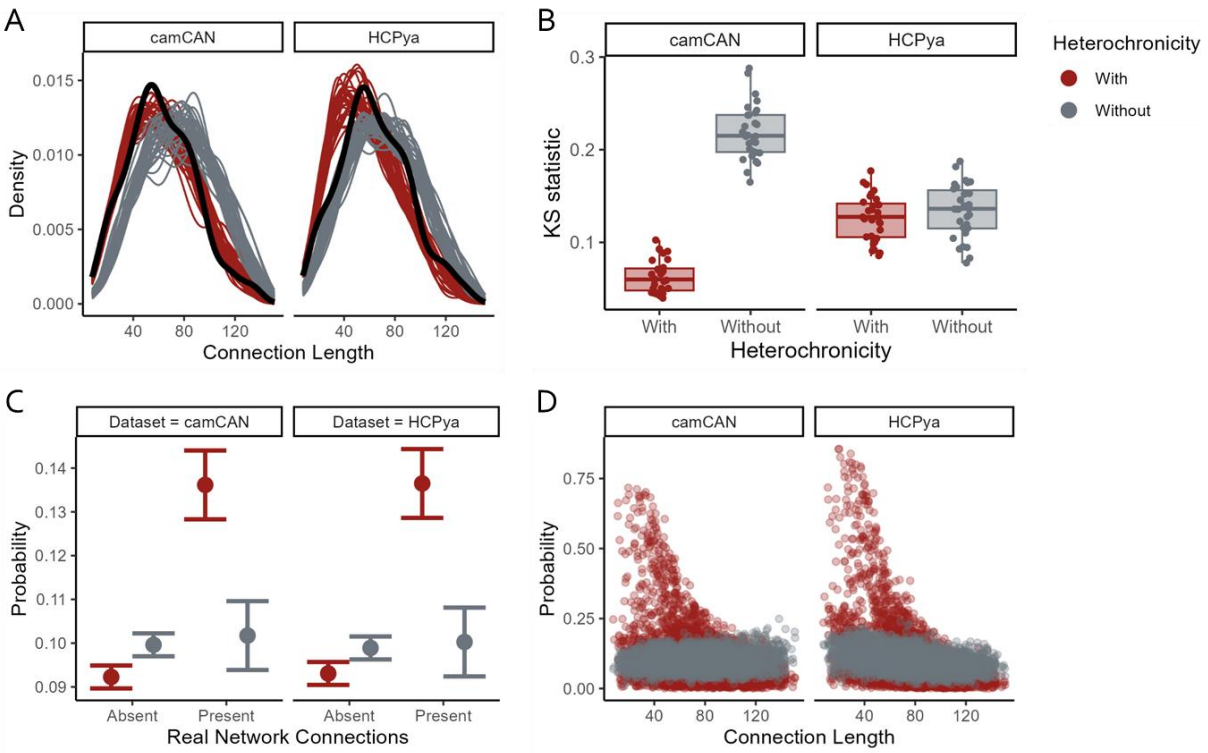

Figure 5. Heterochronous models place correctly only short-range connections. A. The distributions of connection lengths generated by the heterochronous model (red) and the classical model (grey) across individual simulation runs, plotted against the empirical consensus network (black). **B.** Two-sample Kolmogorov–Smirnov (KS) statistics comparing each synthetic network with the empirical distribution. Lower values indicate a closer match. The heterochronous model fits the CamCAN data significantly better than the classical model, whereas no clear difference is observed for the HCP-YA dataset. **C.** Mean probability of drawing edges that are present (right) or absent (left) in the empirical network. In both datasets, heterochronous models outperform classical models at identifying existing connections and rejecting non-existing ones. Error bars show 95 % confidence intervals. **D.** Edge-wise accuracy of the heterochronous (red) and classical (grey) models as a function of connection length. The heterochronous model is accurate for short-range connections but falls to chance for long-range connections, whereas the classical model remains at chance across all distances.

Discussion

Incorporating a spatially heterochronous developmental gradient into generative network models markedly enhances our ability to recreate not only the topology but also the topography of human brain networks. By constraining nodes to make connections following a probabilistic spatiotemporal gradient, the model produces synthetic connectomes whose spatial distributions of graph metrics align far more closely with empirical diffusion-MRI data than classical, temporally agnostic models. This improvement underscores the importance of incorporating temporal aspects of development within computational models of the adult connectome. Likewise, computational models offer a way of empirically formalising and testing developmental theory.

The parameter search consistently pointed to a caudo-rostral wave of connectional maturation: origins located in posterior medial cortex yielded the lowest energy across both the CamCAN and HCPya datasets. This caudal origin point gave occipital and parietal regions more time to connect with other areas, which in turn led them to display high degree. This is consistent with evidence indicating that occipital and parietal regions show more connections in human cortical networks (Hagmann et al., 2008; Kaiser & Varier, 2011). This gradient is also in line with previous work showing earlier

myelination of occipital compared to prefrontal areas (Gao et al., 2009), indicating that a similar gradient might exist beyond connections formation.

At first glance, the result conflicts with dual-origin accounts that posit two independent neurogenetic fronts (e.g., hippocampo-piriform or thalamic-sensorimotor). However, it is important to delineate the purposes of those theories, that is, to explain neurogenesis and laminar differentiation. In contrast, our model is a computational formalisation of the later-emerging pattern of white-matter connectivity. It remains entirely plausible that neurons are born in multiple foci, while axonal growth is coordinated by a single, dominant spatiotemporal program or by distinct programs that are indistinguishable at the spatial resolution of current diffusion imaging. By explicitly modelling different heterochronous gradients for each neurobiological process (e.g., cell birth, axon growth, myelination) we can test whether different principles really exist.

A major strength of the study is replication across independent cohorts, thus increasing our confidence that the heterochronous mechanism is capturing a fundamental organizational principle rather than a dataset-specific artefact. Even so, we caution that both analyses used the AAL parcellation (Gajwani et al., 2023; Zalesky et al., 2010). GNMs on lower resolution parcellations (Akarca et al., 2021; Mousley et al., 2025) have been shown to have better spatial embedding than those at higher resolution (e.g., Zhang et al., 2021), but future work should test whether the caudo-rostral solution persists under higher-resolution or functionally defined atlases.

Despite the overall gains, the model still falls short in capturing the correct long-range connections. Given the repeated failures in simulating these specific connections (Oldham et al., 2025), it is possible that the locations of these connections are simply not established based upon the whole-brain network principles implemented here. Instead it is possible that the locations of these crucial long-range connections are determined by the need to acheive specific idosyncractic functional goals within our evolutionary past. For example, even if the prefrontal-occipital pathway is metabolically expensive, it is essential for top-down modulation of vision, and therefore it might be retained even if it violates the usual principles of wiring economy. Alternatively, the poor fit of the model to long-distance connections might be due to imprecise modelling or data. On one hand, it is possible that these modelling approaches are still incomplete, and introducing new developmental constraints might enhance our ability to map long-range connections (see also Nicosia et al., 2013). On the other hand, most DTI connectomes underweight the probability of long-distance connections due to well-known issues with crossing fibres and higher false-negative rate for long, tenuous pathways maier(Maier-Hein et al., 2017; Thomas et al., 2014). Hence, poorer fit for long connections might reflect limitations in the "gold standard" empirical data rather than shortcomings of the generative model.

Finally, the heterochronous formulation opens the door to modelling individualised developmental trajectories. This is crucial because network formation processes heavily influence both the structural layout of neural circuits and their functional capabilities, impacting cognitive development as well as psychological wellbeing (Schafer et al., 2019; Schnack et al., 2015; Shaw et al., 2007). Prior GNMs have been used to probe group differences (Vértes et al., 2012; Zhang et al., 2021) and individual differences (Akarca et al., 2021), and parameters related to homophily have sometimes been given biological interpretations. However, other terms – most notably the distance penalty – are harder to map onto specific neurodevelopmental mechanisms. In contrast, the heterochronic parameters we introduce (e.g., origin point, strength, temporal dispersion) allows mapping individual differences in best-fitting parameters to clear biological and developmental parameters. It is thus possible to estimate individualised *changes* in brain organization. This could reveal how different trajectories in network formation ultimately lead to diverse network organizations.

Methods

Datasets

The Cambridge Centre for Ageing and Neuroscience (CamCAN) study tracks neuro-cognitive changes across the lifespan (Shafto et al., 2014). Conducted at the MRC Cognition and Brain Sciences Unit, University of Cambridge, it focuses on the neural underpinnings of healthy ageing (see Shafto et al., 2014 for full sample and imaging details). All diffusion-MRI gradient directions (i.e., "b-tables") were validated with an automated quality-control routine to ensure accuracy (Schilling et al., 2019).

The Human Connectome Project – Young Adult (HCPya) dataset was acquired across several sites by the WU–Minn consortium to characterise brain connectivity in a large sample of healthy adults (see Van Essen et al., 2013 for further sample and imaging information). A group-average template was built from 930 participants, and diffusion data were reconstructed in MNI space with q-space diffeomorphic reconstruction (Yeh & Tseng, 2011) to obtain spin-distribution functions (Yeh et al., 2010).

To isolate heterochronicity from broader age-related effects, we confined our analyses to participants aged 26–35 years, thereby avoiding lifespan developmental patterns that could add noise. For this reason, in the present analyses we retained only participants aged 26–35 years, resulting in 78 CamCAN and 829 HCPya individuals.

Data Preprocessing

The data was accessed in a reconstructed format from DSI Studio's Fiber Data Hub (Yeh, 2025). Each participant's structural connectome was then traced with *deterministic* tractography based on generalized q-sampling imaging (GQI) in DSI Studio (Yeh et al., 2010), using the *qsiprep* dsi_studio_gqi workflow (Cieslak et al., 2021). Tractography was seeded in all voxels of the AAL-116 atlas (Tzourio-Mazoyer et al., 2002); subcortical parcels 91–116 were then excluded, yielding the AAL-90 cortical parcellation. Tracking parameters were identical for every participant: 5 million streamlines, seeded at random; step size = 1 mm; turning angle threshold = 35°; minimum / maximum fibre length = 30 mm / 250 mm. Connectivity was quantified with a count-end definition: a streamline contributed to the connection matrix only if it terminated in both of the paired regions. The resulting edge weight—our variable of interest—was the streamline count between each pair of parcels.

Once individual connectomes were obtained, we built a consensus connectome using the *struct_consensus* function from the *netneurotools* package in Python, which relies on the distance-dependent algorithm as implemented by Betzel and colleagues (Betzel et al., 2019). Once a consensus network was created for each dataset, we thresholded it to 10% density based on the strongest connections (Akarca et al., 2021). Finally, the networks where binarised. The resulting consensus networks were in the form of fully connected adjacency matrices.

Computational modelling

Models were generated following equation (4) in the Results section. K, D and H represent the matrices for homophily (i.e., matching index), distance, and heterochronicity, respectively. Homophily was computed as the matching index of the adjacency matrix, which is a measure that quantifies the similarity of input and/or output connections of two nodes excluding their mutual connections (Goñi et al., 2014; Hilgetag et al., 2000; Vértes et al., 2012); Euclidean distance was computed simply by calculating the straight-line distance between the spatial coordinates of node pairs in the anatomical space; Heterochronicity was computed using a time-varying cumulative Gaussian function. More specifically, the likelihood of a certain node i to establish any connection at the time t was given by a Gaussian distribution:

$$h_{it} = \exp(-\frac{(d_i-\mu_t)^2}{2\sigma^2}), \quad (2)$$

where d_i is the Euclidean distance of node i from the origin point, σ is the standard deviation of the Gaussian (which was kept at a fixed value, σ = 15) and μ_t changes across time as follows:

$$\mu_t = \frac{t}{T-1} \cdot \max_i(d_i), \quad (3)$$

thus placing the centre of the Gaussian μ_t at equally spaced positions along the distance axis from the reference point out to the farthest node. Importantly, once a node became "active" (a) and started making connections, it remained active until the end of the heterochronous process, such that:

$$h_{it}^a = \max_{t' \leq t}(h_{it'}), \quad (4)$$

where t' indexes over all previous time steps up to and including t. Once the likelihood of connecting was defined for each node, an undirected matrix could be generated, thus specifying the likelihood of any two nodes i and j of connecting:

$$H_{ij,t} = max(h_{it}^{\mathrm{a}}, h_{jt}^{\mathrm{a}}), \quad (5)$$

A simple representation of this process can be found in Figure 1D.

Model fitting

The models were fitted to the consensus networks to minimize the topological and topographical energies. In the standard energy function, only topology is taken into account. More specifically, the difference in the cumulative distributions of four network metrics between real and synthetic networks is computed in terms of Kolmogormov-Smirnoff (KS) similarity, such that the energy of the synthetic model is computed as follows:

$$\mathrm{Energy}_{\mathrm{tolopogy}} = \max(\mathrm{KS}_d, \mathrm{KS}_b, \mathrm{KS}_c, \mathrm{KS}_l) \quad (6)$$

Where *d* stands for nodal degree, *b* for betweenness centrality, *c* clustering coefficient, and *l* for edge length.

Here, we also considered a topological energy. To compute this energy, we calculated the correlation *r* between the synthetic and actual nodal metrics (i.e., nodal degree, betweenness centrality, clustering coefficient), and took the smallest value as the energy:

$$\mathrm{Energy}_{\mathrm{topography}} = \min(\mathrm{r}_d, \mathrm{r}_b, \mathrm{r}_c) \quad (7)$$

The resulting total energy was a sum of topological and topographical energies, each normalised such that they are weighted equally:

$$\mathrm{Energy}_{\mathrm{total}} = \mathrm{Energy}_{\mathrm{tolopogy}}' + \mathrm{Energy}_{\mathrm{topography}}' \quad (8)$$

Given that we aimed to capture the *approximate* location of the network properties, we performed a spatial smoothing before computing the topographical energy. For a node-level network property X_i, the unnormalised spatial smoothing weights Ω are given by:

$$\Omega_{\mathrm{ij}} = exp(-D_{\mathrm{ij}}^2 / (2\sigma^2)) \quad (9)$$

For each node *i*, a larger weight is assigned to those nodes *j* which are closer to *i* in space (i.e., have a lower value of D_{ij}). The parameter σ controls the spatial scale of the smoothing. These weights do not sum to 1, so we normalise by performing:

$$\Omega_{\mathrm{ij}} = \Omega_{\mathrm{ij}} / \Sigma_{\mathrm{k}} \Omega_{\mathrm{ik}} \qquad (10)$$

The node-level property is then smoothed using these weights to obtain $\Sigma_j \mathbf{\Omega}_{ij} X_j$. The correlation between these smoothed quantities across the real and synthetic networks can then be computed.

When fitting the model, γ, η, and λ (which regulate the impact of homophily *K*, Euclidean distance *D*, and heterochronicity *H*, respectively on the probability of making a connection) were free parameters. More specifically, each of them was free to vary as follows: γ = [0, 0.8], η = [-3.5, 0], and λ = [0, 15]. The ranges of γ and η were based on previous literature (Akarca et al., 2021) while the range of λ was kept broader because no prior knowledge is available.

In addition, the coordinates of the origin point of the heterochronous gradient were also treated as free parameters. In the first analysis, the range of values was defined following the medial plane. First, we found the minimum and maximum *y* and *z* values across all brain coordinates to create a 3D box that fully contains the brain. Next, we sample 9 points in each direction (i.e., 9 along the y axis and 9 along the z axis), evenly spacing sample points across each axis within the bounding box, forming a 2D grid of points. Finally, we checked which of those grid points actually fall inside the brain's shape (not just the box) using a *convex hull* — a geometric wrapper that approximates the outer surface of the brain. The points that fell inside the brain were used as potential origins for heterochronous development. In the subsequent analyses (Figure 4), we used the nodes of the AAL atlas as origin points.

A grid-search was performed over the multidimensional parameters space. For parameters γ, η, and λ, 10 equidistant values were sampled. The medial sweep approach returned 42 valid origin points. This resulted to a total of 42000 parameters combinations. Given that network formation is a stochastic process, we run each combination of parameters 10 times. All network metrics reported in the paper are averaged across runs to reduce noise in the estimates.

The combination of parameters that lead to the lowest energy was similar for the camCAN and the HCPya datasets. For camCAN, the lowest $\mathrm{Energy}_{\mathrm{total}}$ was 0.296 (with $\mathrm{Energy}_{\mathrm{tolopogy}}{}'$ = 0.199 and $\mathrm{Energy}_{\mathrm{topography}}{}'$ = 0.395). The lowest energy was obtained with parameters values η = -1.17, γ = 0.23, and λ = 5.0, and with origin point coordinates y = -66.97 and z = 44.03. For HCPya, the lowest $\mathrm{Energy}_{\mathrm{total}}$ was 0.315 (with $\mathrm{Energy}_{\mathrm{tolopogy}}{}'$ = 0.446 and $\mathrm{Energy}_{\mathrm{topography}}{}'$ = 0.187). The lowest energy was obtained with parameters values η = -1.56, γ = 0.23, and λ = 5.0, and with origin point coordinates y = -66.97 and z = 31.01.

Analysis

All statistical analyses were carried out in R (version 4.2.2), using the *lm* function from the *stats* package.

Acknowledgements

All data provided on DSI Studio were analysed using the US National Science Foundation, ACCESS program, resource allocation (TG-CIS200026) at Extreme Science and Engineering Discovery Environment (XSEDE) resources (Towns, J. et al. Computing in science & engineering 16, 62-74 2014) by Fang-Cheng Yeh at the University of Pittsburgh. **Funding**: This work was supported by the NWO Rubicon grant to F.P. and by the Templeton World Charity Foundation, Inc. (funder DOI 501100011730) under grant TWCF-2022-30510 to D.A.

Author contributions: F.P.: Conceptualization, Methodology, Formal analysis, Data Curation, Writing – Original draft, Visualisation, Funding acquisition; S.O.: Conceptualization, Writing – Review & Editing; A.M.: Data Curation, Writing – Review & Editing; E.T.B.: Conceptualization, Writing – Review & Editing; P.E.V.: Conceptualization, Writing – Review & Editing; D.A.: Conceptualization, Methodology, Resources, Writing – Review & Editing, Supervision, Funding acquisition.

Competing interests: The authors declare that they have no competing interests.

Data and code availability: All data needed to evaluate the conclusions in the paper are present in the paper and/or the Supplementary Materials. Data and code are available on OSF: https://osf.io/2yuh7/overview?view_only=cdd0d4763a484c379b14f2c5a71bd1e8.

References

Achard, S., Salvador, R., Whitcher, B., Suckling, J., & Bullmore, E. D. (2006). A resilient, low-frequency, small-world human brain functional network with highly connected association cortical hubs. *Journal of Neuroscience*, *26*(1), 63–72.

Akarca, D., Vértes, P. E., Bullmore, E. T., & Astle, D. E. (2021). A generative network model of neurodevelopmental diversity in structural brain organization. *Nature Communications*, *12*(1), 4216. https://doi.org/10.1038/s41467-021-24430-z

Arnatkeviciute, A., Fulcher, B. D., Oldham, S., Tiego, J., Paquola, C., Gerring, Z., Aquino, K., Hawi, Z., Johnson, B., & Ball, G. (2021). Genetic influences on hub connectivity of the human connectome. *Nature Communications*, *12*(1), 4237.

Bassett, D. S., & Bullmore, E. (2006). Small-World Brain Networks. *The Neuroscientist*, *12*(6), 512–523. https://doi.org/10.1177/1073858406293182

Betzel, R. F., Avena-Koenigsberger, A., Goñi, J., He, Y., De Reus, M. A., Griffa, A., Vértes, P. E., Mišic, B., Thiran, J.-P., & Hagmann, P. (2016). Generative models of the human connectome. *Neuroimage*, *124*, 1054–1064.

Betzel, R. F., Griffa, A., Hagmann, P., & Mišić, B. (2019). Distance-dependent consensus thresholds for generating group-representative structural brain networks. *Network Neuroscience*, *3*(2), 475–496.

Bullmore, E., & Sporns, O. (2009). Complex brain networks: Graph theoretical analysis of structural and functional systems. *Nature Reviews Neuroscience*, *10*(3), 186–198.

Bullmore, E., & Sporns, O. (2012). The economy of brain network organization. *Nature Reviews Neuroscience*, *13*(5), 336–349.

Carozza, S., Akarca, D., & Astle, D. (2023). The adaptive stochasticity hypothesis: Modeling equifinality, multifinality, and adaptation to adversity. *Proceedings of the National Academy of Sciences of the United States of America*, *120*(42), e2307508120. https://doi.org/10.1073/pnas.2307508120

Carozza, S., Holmes, J., Akarca, D., & Astle, D. E. (2024). Global topology of human connectome is insensitive to early life environments–A prospective longitudinal study of the general population. *Developmental Science*, e13490.

Cieslak, M., Cook, P. A., He, X., Yeh, F.-C., Dhollander, T., Adebimpe, A., Aguirre, G. K., Bassett, D. S., Betzel, R. F., & Bourque, J. (2021). QSIPrep: An integrative platform for preprocessing and reconstructing diffusion MRI data. *Nature Methods*, *18*(7), 775–778.

Finlay, B. L., & Uchiyama, R. (2015). Developmental mechanisms channeling cortical evolution. *Trends in Neurosciences*, *38*(2), 69–76.

Finlay, B. L., & Uchiyama, R. (2020). Chapter 34—The Timing of Brain Maturation, Early Experience, and the Human Social Niche. In J. H. Kaas (Ed.), *Evolutionary Neuroscience (Second Edition)* (pp. 815–843). Academic Press. https://doi.org/10.1016/B978-0-12-820584-6.00034-9

Gajwani, M., Oldham, S., Pang, J. C., Arnatkevičiūtė, A., Tiego, J., Bellgrove, M. A., & Fornito, A. (2023). Can hubs of the human connectome be identified consistently with diffusion MRI? *Network Neuroscience*, *7*(4), 1326–1350. https://doi.org/10.1162/netn_a_00324

Gao, W., Lin, W., Chen, Y., Gerig, G., Smith, J. K., Jewells, V., & Gilmore, J. H. (2009). Temporal and spatial development of axonal maturation and myelination of white matter in the developing brain. *American Journal of Neuroradiology*, *30*(2), 290–296.

Gogtay, N., Giedd, J. N., Lusk, L., Hayashi, K. M., Greenstein, D., Vaituzis, A. C., Nugent, T. F., Herman, D. H., Clasen, L. S., Toga, A. W., Rapoport, J. L., & Thompson, P. M. (2004). Dynamic mapping of human cortical development during childhood through early adulthood. *Proceedings of the National Academy of Sciences*, *101*(21), 8174–8179. https://doi.org/10.1073/pnas.0402680101

Gong, G., He, Y., Concha, L., Lebel, C., Gross, D. W., Evans, A. C., & Beaulieu, C. (2009). Mapping anatomical connectivity patterns of human cerebral cortex using in vivo diffusion tensor imaging tractography. *Cerebral Cortex*, *19*(3), 524–536.

Goñi, J., Van Den Heuvel, M. P., Avena-Koenigsberger, A., Velez De Mendizabal, N., Betzel, R. F., Griffa, A., Hagmann, P., Corominas-Murtra, B., Thiran, J.-P., & Sporns, O. (2014). Resting-brain functional connectivity predicted by analytic measures of network communication. *Proceedings of the National Academy of Sciences*, *111*(2), 833–838. https://doi.org/10.1073/pnas.1315529111

Goulas, A., Betzel, R. F., & Hilgetag, C. C. (2019). Spatiotemporal ontogeny of brain wiring. *Science Advances*, *5*(6), eaav9694. https://doi.org/10.1126/sciadv.aav9694

Goulas, A., Majka, P., Rosa, M. G., & Hilgetag, C. C. (2019). A blueprint of mammalian cortical connectomes. *PLoS Biology*, *17*(3), e2005346.

Goulas, A., Margulies, D. S., Bezgin, G., & Hilgetag, C. C. (2019). The architecture of mammalian cortical connectomes in light of the theory of the dual origin of the cerebral cortex. *Cortex*, *118*, 244–261.

Hagmann, P., Cammoun, L., Gigandet, X., Meuli, R., Honey, C. J., Wedeen, V. J., & Sporns, O. (2008). Mapping the structural core of human cerebral cortex. *PLoS Biology*, *6*(7), e159.

Hilgetag, C., Burns, G. A. P. C., O'Neill, M. A., Scannell, J. W., & Young, M. P. (2000). Anatomical connectivity defines the organization of clusters of cortical areas in the macaque and the cat. *Philosophical Transactions of the Royal Society of London. Series B: Biological Sciences*, *355*(1393), 91–110. https://doi.org/10.1098/rstb.2000.0551

Kaiser, M. (2017). Mechanisms of connectome development. *Trends in Cognitive Sciences*, *21*(9), 703–717.

Kaiser, M., & Hilgetag, C. C. (2004a). Modelling the development of cortical systems networks. *Neurocomputing*, *58*, 297–302.

Kaiser, M., & Hilgetag, C. C. (2004b). Spatial growth of real-world networks. *Physical Review E*, *69*(3). https://doi.org/10.1103/physreve.69.036103

Kaiser, M., & Varier, S. (2011). Evolution and development of Brain Networks: From ***Caenorhabditis elegans*** to ***Homo sapiens*** . *Network: Computation in Neural Systems*, *22*(1–4), 143–147. https://doi.org/10.3109/0954898X.2011.638968

Liu, Y., Seguin, C., Mansour, S., Oldham, S., Betzel, R., Di Biase, M. A., & Zalesky, A. (2023). Parameter estimation for connectome generative models: Accuracy, reliability, and a fast parameter fitting method. *NeuroImage*, *270*, 119962.

Maier-Hein, K. H., Neher, P. F., Houde, J.-C., Côté, M.-A., Garyfallidis, E., Zhong, J., Chamberland, M., Yeh, F.-C., Lin, Y.-C., & Ji, Q. (2017). The challenge of mapping the human connectome based on diffusion tractography. *Nature Communications*, *8*(1), 1349.

Mousley, A., Bethlehem, R., Yeh, F.-C., & Astle, D. (2025). *Topological turning points across the human lifespan*. https://2024.ccneuro.org/pdf/11_Paper_authored_Mousley_CCN.pdf

Nicosia, V., Vértes, P. E., Schafer, W. R., Latora, V., & Bullmore, E. T. (2013). Phase transition in the economically modeled growth of a cellular nervous system. *Proceedings of the National Academy of Sciences*, *110*(19), 7880–7885. https://doi.org/10.1073/pnas.1300753110

Oldham, S., & Fornito, A. (2019). The development of brain network hubs. *Developmental Cognitive Neuroscience*, *36*, 100607.

Oldham, S., & Fornito, A. (2023). Hubs and rich clubs. In *Connectome Analysis* (pp. 123–147). Elsevier. https://www.sciencedirect.com/science/article/pii/B9780323852807000154

Oldham, S., Fornito, A., & Ball, G. (2025). Coming up short: Generative network models fail to accurately capture long-range connectivity. *Network Neuroscience*, 1–41.

Oldham, S., Fulcher, B. D., Aquino, K., Arnatkevičiūtė, A., Paquola, C., Shishegar, R., & Fornito, A. (2022). Modeling spatial, developmental, physiological, and topological constraints on human brain connectivity. *Science Advances*, *8*(22), eabm6127. https://doi.org/10.1126/sciadv.abm6127

Pandya, D., Petrides, M., & Cipolloni, P. B. (2015). *Cerebral cortex: Architecture, connections, and the dual origin concept*. Oxford University Press. https://books.google.com/books?hl=en&lr=&id=ctsACgAAQBAJ&oi=fnd&pg=PR3&dq=pandya+dual+origin&ots=s8SZJv-Odj&sig=xLQ-5G1U8IKyUvCfkTqIymRughw

Rolls, E. T., Huang, C.-C., Lin, C.-P., Feng, J., & Joliot, M. (2020). Automated anatomical labelling atlas 3. *Neuroimage*, *206*, 116189.

Schafer, S. T., Paquola, A. C. M., Stern, S., Gosselin, D., Ku, M., Pena, M., Kuret, T. J. M., Liyanage, M., Mansour, A. A., Jaeger, B. N., Marchetto, M. C., Glass, C. K., Mertens, J., & Gage, F. H. (2019). Pathological priming causes developmental gene network heterochronicity in autistic subject-derived neurons. *Nature Neuroscience*, *22*(2), 243–255. https://doi.org/10.1038/s41593-018-0295-x

Schilling, K. G., Yeh, F.-C., Nath, V., Hansen, C., Williams, O., Resnick, S., Anderson, A. W., & Landman, B. A. (2019). A fiber coherence index for quality control of B-table orientation in diffusion MRI scans. *Magnetic Resonance Imaging*, *58*, 82–89.

Schnack, H. G., van Haren, N. E. M., Brouwer, R. M., Evans, A., Durston, S., Boomsma, D. I., Kahn, R. S., & Hulshoff Pol, H. E. (2015). Changes in Thickness and Surface Area of the Human Cortex and Their Relationship with Intelligence. *Cerebral Cortex*, *25*(6), 1608–1617. https://doi.org/10.1093/cercor/bht357

Sebenius, I., Dorfschmidt, L., Seidlitz, J., Alexander-Bloch, A., Morgan, S. E., & Bullmore, E. (2025). Structural MRI of brain similarity networks. *Nature Reviews Neuroscience*, *26*(1), 42–59.

Sebenius, I., Warrier, V., Bethlehem, R. A., Dear, R., Stauffer, E.-M., Gu, Y., Romero-Garcia, R., Seidlitz, J., Bullmore, E., & Morgan, S. (2024). The genetic architecture of cortical similarity networks. *BioRxiv*, 2024–12.

Shafto, M. A., Tyler, L. K., Dixon, M., Taylor, J. R., Rowe, J. B., Cusack, R., Calder, A. J., Marslen-Wilson, W. D., Duncan, J., Dalgleish, T., Henson, R. N., Brayne, C., Matthews, F. E., & Cam-CAN. (2014). The Cambridge Centre for Ageing and Neuroscience (Cam-CAN) study protocol: A cross-sectional, lifespan, multidisciplinary examination of healthy cognitive ageing. *BMC Neurology*, *14*(1), 204. https://doi.org/10.1186/s12883-014-0204-1

Shaw, P., Eckstrand, K., Sharp, W., Blumenthal, J., Lerch, J. P., Greenstein, D., Clasen, L., Evans, A., Giedd, J., & Rapoport, J. L. (2007). Attention-deficit/hyperactivity disorder is characterized by a delay in cortical maturation. *Proceedings of the National Academy of Sciences*, *104*(49), 19649–19654. https://doi.org/10.1073/pnas.0707741104

Sporns, O., & Betzel, R. F. (2016). Modular Brain Networks. *Annual Review of Psychology*, *67*(1), 613–640. https://doi.org/10.1146/annurev-psych-122414-033634

Thomas, C., Ye, F. Q., Irfanoglu, M. O., Modi, P., Saleem, K. S., Leopold, D. A., & Pierpaoli, C. (2014). Anatomical accuracy of brain connections derived from diffusion MRI tractography is inherently limited. *Proceedings of the National Academy of Sciences*, *111*(46), 16574–16579. https://doi.org/10.1073/pnas.1405672111

Tzourio-Mazoyer, N., Landeau, B., Papathanassiou, D., Crivello, F., Etard, O., Delcroix, N., Mazoyer, B., & Joliot, M. (2002). Automated anatomical labeling of activations in SPM using a macroscopic anatomical parcellation of the MNI MRI single-subject brain. *Neuroimage*, *15*(1), 273–289.

Van Den Heuvel, M. P., & Sporns, O. (2011). Rich-club organization of the human connectome. *Journal of Neuroscience*, *31*(44), 15775–15786.

Van Essen, D. C., Smith, S. M., Barch, D. M., Behrens, T. E., Yacoub, E., Ugurbil, K., & Consortium, W.-M. H. (2013). The WU-Minn human connectome project: An overview. *Neuroimage*, *80*, 62–79.

Vértes, P. E., Alexander-Bloch, A. F., Gogtay, N., Giedd, J. N., Rapoport, J. L., & Bullmore, E. T. (2012). Simple models of human brain functional networks. *Proceedings of the National Academy of Sciences*, *109*(15), 5868–5873. https://doi.org/10.1073/pnas.1111738109

Yeh, F.-C. (2025). DSI Studio: An integrated tractography platform and fiber data hub for accelerating brain research. *Nature Methods*, 1–3.

Yeh, F.-C., & Tseng, W.-Y. I. (2011). NTU-90: A high angular resolution brain atlas constructed by q-space diffeomorphic reconstruction. *Neuroimage*, *58*(1), 91–99.

Yeh, F.-C., Wedeen, V. J., & Tseng, W.-Y. I. (2010). Generalized q-Sampling Imaging. *IEEE Transactions on Medical Imaging*, *29*(9), 1626–1635. https://doi.org/10.1109/TMI.2010.2045126

Yeterian, E. H., Pandya, D. N., Tomaiuolo, F., & Petrides, M. (2012). The cortical connectivity of the prefrontal cortex in the monkey brain. *Cortex*, *48*(1), 58–81.

Zalesky, A., Fornito, A., Harding, I. H., Cocchi, L., Yücel, M., Pantelis, C., & Bullmore, E. T. (2010). Whole-brain anatomical networks: Does the choice of nodes matter? *NeuroImage*, *50*(3), 970–983. https://doi.org/10.1016/j.neuroimage.2009.12.027

Zhang, X., Braun, U., Harneit, A., Zang, Z., Geiger, L. S., Betzel, R. F., Chen, J., Schweiger, J. I., Schwarz, K., & Reinwald, J. R. (2021). Generative network models of altered structural brain connectivity in schizophrenia. *Neuroimage*, *225*, 117510.

.